Chem

Article

Fine-tuned coordination environment of Pt-Fe-Pt active site for selective heterogeneous hydrogenation of crotonaldehyde

Graphical abstract

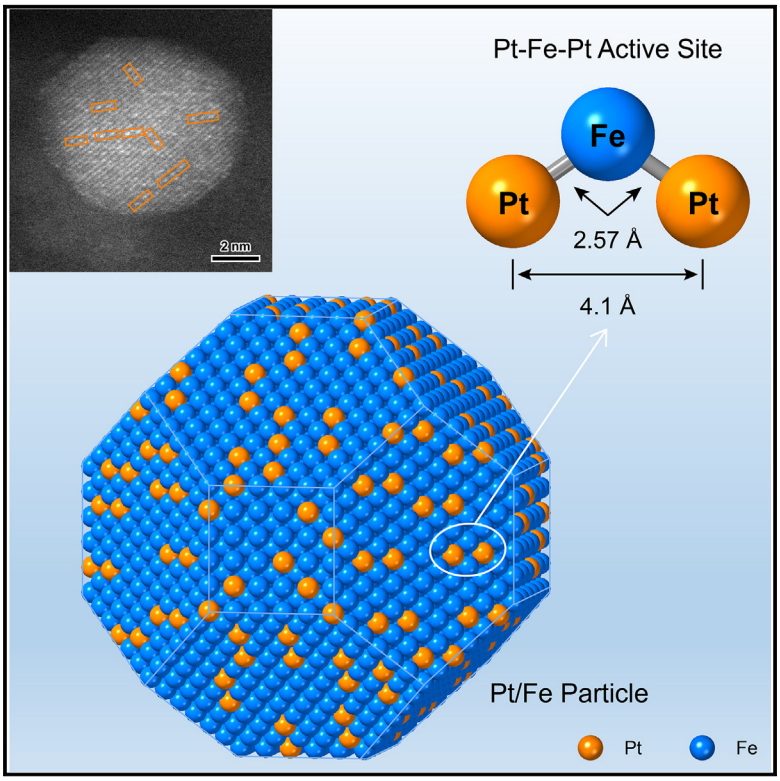

Highlights

- Coupling two Pt atoms with an Fe atom tunes the coordination environment of active site
- Pt-Fe-Pt heterotrimer catalyzes preferential hydrogenation of C=O bond at high activity
- Pt and Fe atoms act in a targeted and synergistic manner via site-bond recognition

Authors

Di Zhou, Junjun Wang, Minzhen Jian, ..., Wei-Xue Li, Yuemin Wang, Wenjie Shen

Correspondence

yongli@dicp.ac.cn (Y.L.), wxli70@ustc.edu.cn (W.-X.L.), yuemin.wang@kit.edu (Y.W.), shen98@dicp.ac.cn (W.S.)

In brief

Densely populating and precisely arranging Pt atoms in the form of Pt-Fe-Pt over an Fe particle not only maximizes the utilization of the costly noble metal for catalysis but also enables the promotion of the overall reaction efficiency. The Pt-Fe-Pt heterotrimer catalyzes the preferential hydrogenation of C=O and simultaneously increases the reaction rate by 35-fold. The fine-tuned coordination environment of Pt-Fe-Pt allows the metal atoms to interact specifically with the functional groups in the reacting molecules and thereby circumvents the activity-selectivity trade-off.

Zhou et al., 2025, Chem *11*, 102380
May 8, 2025
https://doi.org/10.1016/j.chempr.2024.11.018

CellPress

Please cite this article in press as: Zhou et al., Fine-tuned coordination environment of Pt-Fe-Pt active site for selective heterogeneous hydrogenation of crotonaldehyde, Chem (2024), https://doi.org/10.1016/j.chempr.2024.11.018

Chem

CellPress

Article

Fine-tuned coordination environment of Pt-Fe-Pt active site for selective heterogeneous hydrogenation of crotonaldehyde

Di Zhou,[1,6] Junjun Wang,[2,6] Minzhen Jian,[3,6] Yong Li,[1,*] Zheng Jiang,[4] Shuang Liu,[1] Yan Zhou,[1] Jiake Wei,[1] Christof Wöll,[2] Wei-Xue Li,[3,5,*] Yuemin Wang,[2,*] and Wenjie Shen[1,7,*]

[1]State Key Laboratory of Catalysis, Dalian Institute of Chemical Physics, Chinese Academy of Sciences, Dalian 116023, China
[2]Institute of Functional Interfaces, Karlsruhe Institute of Technology, 76344 Eggenstein-Leopoldshafen, Germany
[3]Key Laboratory of Precision and Intelligent Chemistry, Department of Chemical Physics, University of Science and Technology of China, Hefei 230026, China
[4]National Synchrotron Radiation Laboratory, University of Science and Technology of China, Hefei 230026, China
[5]Hefei National Laboratory, University of Science and Technology of China, Hefei 230026, China
[6]These authors contributed equally
[7]Lead contact
*Correspondence: yongli@dicp.ac.cn (Y.L.), wxli70@ustc.edu.cn (W.-X.L.), yuemin.wang@kit.edu (Y.W.), shen98@dicp.ac.cn (W.S.)
https://doi.org/10.1016/j.chempr.2024.11.018

THE BIGGER PICTURE Downsizing noble-metal particles to subnanometric clusters and ultimately to single atoms allows the geometric exposure of almost all noble-metal atoms for catalysis but concomitantly alters the electronic structure of the active site and hence compromises the intrinsic activity and/or selectivity. Coupling two noble-metal atoms via a base-metal atom in bimetallic catalysts creates electron-enriched and electron-deficient sites that could distinguishably activate the functional groups in the reacting molecules. However, experimental fabrication of such an atomically precise active site poses a significant challenge. This work reports an approach to densely populating and precisely arranging Pt atoms in the form of Pt-Fe-Pt over an Fe particle via H_2 reduction at 673 K of a Pt-Fe_2O_3 particle pair, wherein a 3.3 nm Pt particle sits on a 9.8 nm Fe_2O_3 particle. The Fe nanoparticle thus formed disperses the Pt particle into spatially isolated Pt atoms that are chemically bridged by an Fe atom in intermetallic bonds. The Pt-Fe-Pt active site not only catalyzes preferential hydrogenation of the C=O bond, leaving the conjugated C=C bond intact, but also enhances the activity by 35-fold, circumventing the selectivity-activity trade-off that is commonly encountered in selective heterogeneous hydrogenation. The concurrent enhancement in activity and selectivity stems from the fine-tuned coordination environment of the Pt-Fe-Pt active site interacting with the reacting molecules in a site-bond recognition manner, analogous to enzyme catalysis. The left-end Pt atom anchors the C=C bond, whereas the central Fe atom activates the C=O bond, which is further hydrogenated by H atoms supplied by the right-end Pt atom. This finding demonstrates that elegant catalysis necessitates site-bond recognitions between the metal atoms in the active site and the functional groups in the reacting molecules. It would be applicable to a wide range of bimetallic catalysts for selectivity control in the production of fine and specialty chemicals by active-site design at atomic precision.

SUMMARY

Dispersing the catalytically more active noble metal at the single-site scale ensures maximum atom efficiency for selective heterogeneous hydrogenation over bimetallic particles. However, the low density and random location of the noble-metal atoms compromise the intrinsic activity and/or selectivity because of the resulting altered electronic structure. Here, we report that densely populating and precisely arranging Pt atoms in the form of a Pt-Fe-Pt heterotrimer not only catalyzes preferential hydrogenation of the C=O bond in crotonaldehyde (CAL) but also increases the reaction rate by 35-fold, circumventing the activity-selectivity trade-off. The Pt-Fe-Pt active site is fabricated by H_2 reduction at 673 K of a Pt-Fe_2O_3 particle pair, wherein a 3.3 nm Pt particle sits on a 9.8 nm Fe_2O_3 particle. It interacts with the CAL molecule in a site-bond recognition manner: the left-end Pt atom anchors the C=C bond, whereas the central Fe atom activates the C=O bond, which is further hydrogenated by H atoms adsorbed on the right-end Pt atom.

Please cite this article in press as: Zhou et al., Fine-tuned coordination environment of Pt-Fe-Pt active site for selective heterogeneous hydrogenation of crotonaldehyde, Chem (2024), https://doi.org/10.1016/j.chempr.2024.11.018

INTRODUCTION

Active and selective heterogeneous hydrogenation necessitates accurate site-bond recognition at the molecular level, wherein the active sites interact specifically with the functional groups in the reacting molecules.[1] Ideally, only the target functional group is hydrogenated, whereas all other unsaturated bonds are preserved. Bimetallic nanoparticles, consisting of a noble metal and a base metal, feature unique catalysis for selective heterogeneous hydrogenation reactions.[2–4] The distinct geometric and electronic structure of the active site, stemming from the metal-metal interaction, favors the facile activation of H_2 and facilitates the preferential adsorption of the reacting molecule. They traditionally present as bulk alloys, wherein the two types of metal atoms arrange either randomly in the disordered crystal phases or periodically in the ordered intermetallics, but only the noble-metal atoms located on the surface layer are accessible for catalysis.[4] To efficiently utilize the costly noble metals in catalysis, researchers have demonstrated atomically dispersed active sites by downsizing the bimetallic nanoparticles to subnanometric clusters[3–8] and ultimately to single-atom alloys (SAAs).[9–11] This allows almost all noble-metal atoms to be geometrically exposed to the reacting molecules, but the low density and/or random location of the noble-metal atoms alters the electronic character, compromising the selectivity and/or activity.[3,12] Subnanometric clusters, where a few metal atoms are closely located at full dispersion, enable the adjacent atoms to act cooperatively.[5,8] However, the randomly arranged noble-metal atoms, because of the much lower crystallinity,[6,13] have lower selectivity. On the other hand, noble-metal atoms, dispersed in SAAs, feature high selectivity for heterogeneous hydrogenation via the site-decoupling effect.[10,11] But the inherent low surface density at traceable loading amounts limits the overall activity and the ability to catalyze reactions, necessitating multiple sites nearby.[14–20]

The coupling of two noble-metal atoms through a bridging base-metal atom allows flexible accommodation of the reacting molecule and fine-tuning of the electronic character to specifically activate the target functional group. However, the fabrication of such an atomically accurate active site is experimentally challenging. Here, we report an approach to densely populating and accurately locating Pt atoms in the form of Pt-Fe-Pt heterotrimer on an α-Fe nanoparticle. By tracking the H_2 reduction of the Pt-Fe_2O_3 particle pair (a 3.3 nm Pt particle sits on a 9.8 nm Fe_2O_3 particle) with environmental scanning transmission electron microscopy (ESTEM) and *in situ* infrared (IR) spectroscopy, we reveal that α-Fe, derived from Fe_2O_3, disperses the Pt particle into Pt-Fe-Pt heterotrimers in intermetallic bonds. We demonstrate that the Pt-Fe-Pt active site not only selectively catalyzes hydrogenation of the C=O bond in crotonaldehyde (CAL) while preserving the conjugated C=C bond but also enhances the reaction rate dramatically. This overcomes the selectivity-activity trade-off that is commonly encountered in selective heterogeneous hydrogenation. On the basis of comprehensive structure characterizations, kinetic evaluations, and density functional theory (DFT) calculations, we identify the coordination environment of the Pt-Fe-Pt active site and its catalytic mechanism at atomic and molecular levels. It involves well-matched geometric and electronic structures between the metal atoms in the active site and the functional groups in the reacting molecules. Namely, a site-bond recognition pattern is analogous to the lock-and-key model in enzyme catalysis.[21,22] The left-end Pt atom anchors the C=C bond while the central Fe atom activates the C=O bond, which is further hydrogenated by H atoms supplied by the right-end Pt atom. This result elucidates the interactions between the active site and the reacting molecule in terms of both geometric and electronic factors, enabling precise control of the chemical reaction on the solid catalyst surface. It also offers a strategy for tuning the coordination environment of the active site with atomic precision on bimetallic catalysts for selectivity control in heterogeneous hydrogenation reactions.

RESULTS

Preferential hydrogenation of C=O bond over the Pt/Fe catalyst

We first successfully synthesized the Pt-Fe_2O_3 particle pair that was deposited onto a high-surface-area silica support (Figure S1). The Pt loading amount was 0.9 wt %, whereas that of Fe was 4.2 wt %, approximately equal to a Pt/Fe atomic ratio of 1/16. High-angle annular dark-field scanning transmission electron microscopy (HAADF-STEM) showed that the particle pairs were separated at a distance of 9.4 nm on average over silica (Figure 1A). In each particle pair, a 3.3 nm Pt particle sat on a 9.8 nm Fe_2O_3 particle (Figures 1B and S1G–S1I). The two lattice spacings of 0.482 nm, at a dihedral angle of 70.5°, indicated γ-Fe_2O_3{111} planes, whereas the two lattice spacings of 0.227 nm, at a dihedral angle of 70.5°, referred to Pt{111} planes. Energy-dispersive X-ray (EDX) element mappings confirmed Pt-Fe_2O_3 proximity in the particle-pair geometry (Figure 1C). X-ray absorption spectroscopy (XAS) spectra resolved the coordination environments of Pt and Fe in the Pt-Fe_2O_3 particle pair. At the Pt L_3-edge, the normalized X-ray absorption near-edge structure (XANES) spectrum showed a white-line intensity located between the PtO_2 and Pt foils (Figure S2A), characteristic of PtO_x.[23] The Fourier transform extended X-ray absorption fine structure (EXAFS) spectrum consisted of multiple scattering paths at 1.0–3.1 Å (Figure 1D), including a Pt–O path with a distance of 2.0 Å in PtO_x and a Pt–Pt path with a length of 2.76 Å in the Pt particle.[23] At the Fe K-edge, the pre-edge peak in the XANES spectrum showed Fe_2O_3 (Figure S2B), whereas the EXAFS scattering paths at 0.9–3.7 Å (Figure 1E) indicated Fe–O and Fe–Fe bonds.[24]

The Pt-Fe_2O_3 particle pair was then subjected to H_2 reduction at 673 K, during which the transformation of Fe_2O_3 to α-Fe dispersed the Pt particle into isolated Pt atoms (Figure 2A). We note that the substantial spatial distance between the particle pairs ensured that the H_2 reduction occurred at a single-particle-pair scale, as demonstrated by recent experimental investigations.[25,26] A primary temperature-programmed hydrogen reduction experiment showed that the Fe_2O_3 particle was reduced first to Fe_3O_4 at 473 K and then to α-Fe at 673 K, whereas the corresponding *in situ* X-ray photoelectron spectroscopy (XPS) and X-ray diffraction (XRD) data attested to the formation of Fe_3O_4 and α-Fe at the respective temperatures (Figure S3). Accordingly, we first treated the Pt-Fe_2O_3 particle

Please cite this article in press as: Zhou et al., Fine-tuned coordination environment of Pt-Fe-Pt active site for selective heterogeneous hydrogenation of crotonaldehyde, Chem (2024), https://doi.org/10.1016/j.chempr.2024.11.018

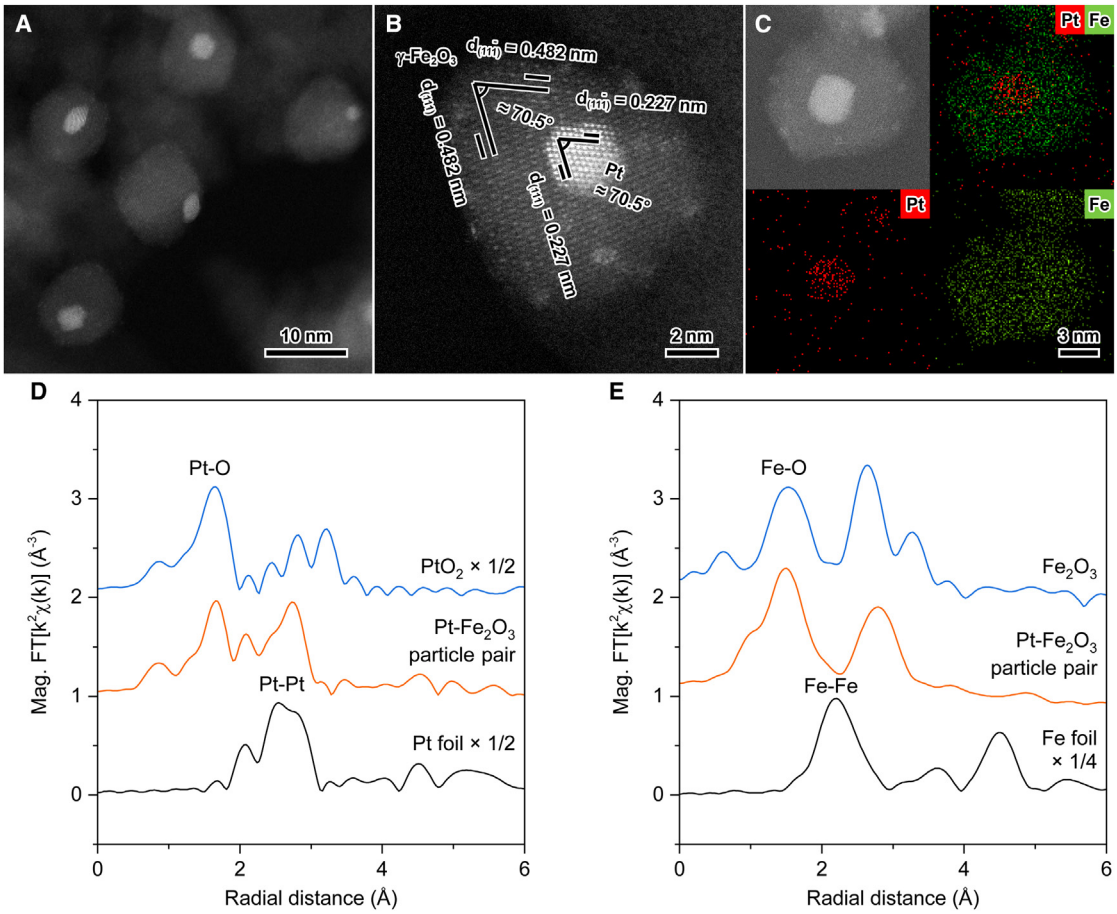

Figure 1. Structure of the Pt-Fe_2O_3 particle pair

(A and B) STEM images.

(C) EDX element mappings.

(D and E) k^2-weighted Fourier transform EXAFS spectra at the Pt L_3-edge (D) and Fe K-edge (E).

pair with H_2 at 473 K for 2 h to yield the Pt/Fe_3O_4 catalyst. STEM images identified that a 3.3 nm Pt particle epitaxially grew on a 9.6 nm Fe_3O_4 particle in this sample (Figure S4). To further convert Fe_3O_4 to α-Fe, we reduced the Pt-Fe_2O_3 particle pair with H_2 at 673 K for 2 h, giving the Pt/Fe catalyst. However, the geometric arrangements of Pt and Fe atoms in this sample could not be resolved by routine STEM because the metallic Fe was immediately oxidized upon exposure to air and/or moisture during sample handling because of its high oxygen affinity.[27] Environmental STEM (ESTEM) experiments that directly visualized the structural evolution of the Pt-Fe_2O_3 particle pair in H_2 at high temperatures demonstrated that the Pt atoms were spatially isolated on the α-Fe nanoparticle in the form of Pt-Fe-Pt heterotrimer, as will be discussed later.

We elucidated the coordination environments of Pt and Fe in the two catalysts by *in situ* XAS. The XANES spectra verified the chemical states of Pt and Fe. The white lines at the Pt L_3-edge for both samples resembled that for the Pt foil (Figure S5A), indicating their metallic nature in general. The spectra at the Fe K-edge identified Fe_3O_4 in the Pt/Fe_3O_4 sample but α-Fe in the Pt/Fe catalyst (Figure S5B). The EXAFS spectra quantified the coordination environments of Pt and Fe (Figures 2B, 2C, and S5C–S5K). For the Pt/Fe_3O_4 catalyst, the Fourier transform spectrum at the Fe K-edge displayed Fe–O (2.01 Å), Fe–Fe_1 (3.02 Å), and Fe–Fe_2 (3.50 Å) scattering paths with coordination numbers (CNs) of 5.3, 5.7, and 5.2, respectively, characteristics of Fe_3O_4.[28] The spectrum at the Pt L_3-edge consisted of Pt–Pt and Pt–Fe paths. The Pt–Pt path had a distance of 2.76 Å with a CN of 9.2, typical for the Pt particle; the Pt–Fe path had a shorter length of 2.63 Å with a CN of 1.7, referring to the interfacial Pt atoms connected to Fe_3O_4 surface.[23] For the Pt/Fe catalyst, the Fe K-edge spectrum included Fe–Fe paths with distances of 2.47 Å (CN = 5.4) and 2.86 Å (CN = 4.0), demonstrating the body-centered cubic α-Fe.[24] The Pt L_3-edge spectrum contained two Pt-Fe paths at distances of 2.57 Å (Pt–Fe_1, CN = 7.9) and 2.86 Å (Pt–Fe_2, CN = 3.9), referring to Pt coordinations to the first and second nearest shells of α-Fe,[15,29] respectively. No Pt–Pt paths could be resolved in the first or second coordination shells, suggesting the atomically dispersed Pt. We visualized the coordinations of Pt to Fe by depicting a unit cell of α-Fe with one substituted Pt atom (Figure 2D), whose first and second nearest neighbors to Fe had bond lengths of 2.57 and 2.86 Å,

Please cite this article in press as: Zhou et al., Fine-tuned coordination environment of Pt-Fe-Pt active site for selective heterogeneous hydrogenation of crotonaldehyde, Chem (2024), https://doi.org/10.1016/j.chempr.2024.11.018

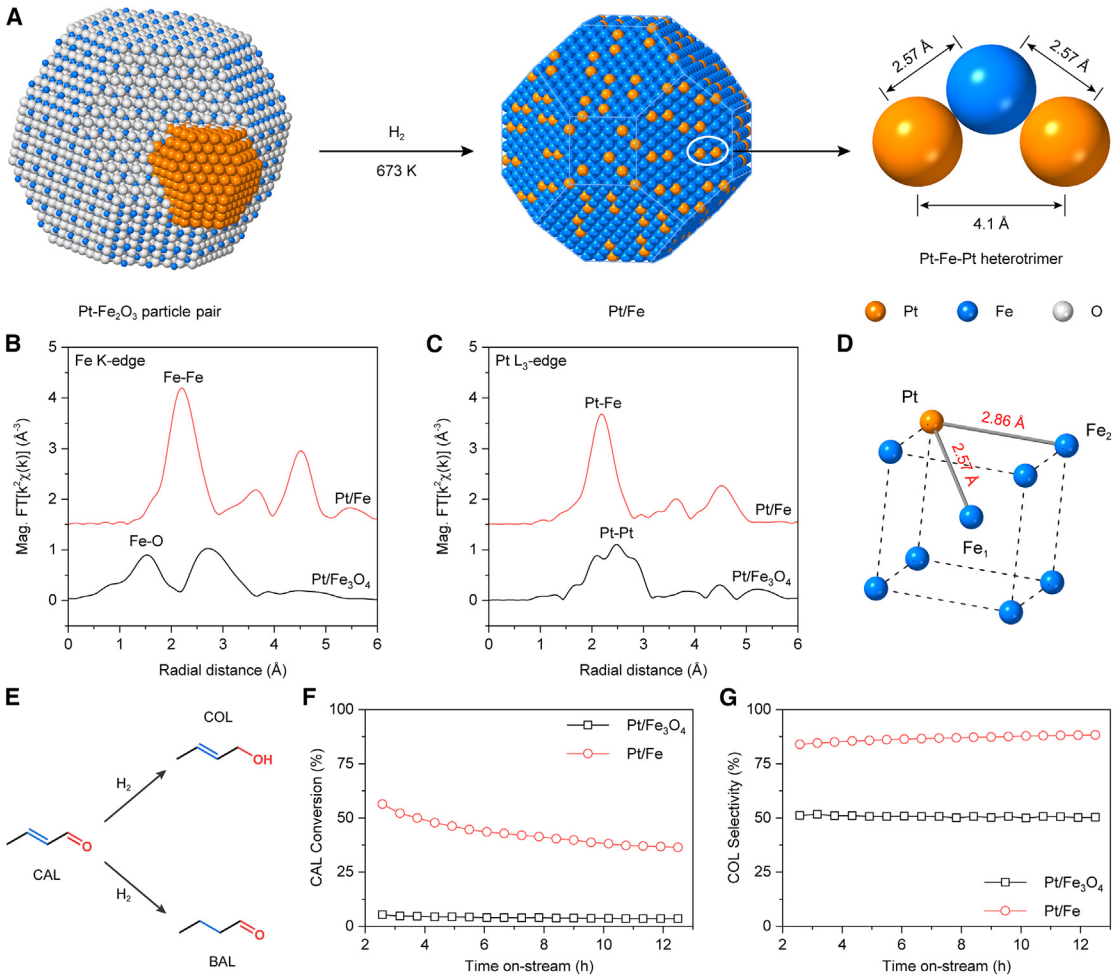

Figure 2. Crotonaldehyde hydrogenation over the Pt catalysts at 353 K

(A) Schematic illustrations of the fabrication of the Pt/Fe catalyst and the geometry of the Pt-Fe-Pt heterotrimer.

(B and C) k^2-weighted Fourier transform EXAFS spectra at the Fe K-edge (B) and Pt L_3-edge (C).

(D) Pt–Fe bonds in the unit cell of α-Fe.

(E) Competitive hydrogenation of C=O and C=C bonds in CAL.

(F and G) CAL conversion (F) and COL selectivity (G) over the Pt catalysts.

respectively. These XAS data showed that the Pt particle in the Pt-Fe_2O_3 particle pair, upon H_2 reduction at 673 K, dispersed into isolated Pt atoms in the Pt/Fe catalyst.

We subsequently tested the Pt catalysts for the gas-phase hydrogenation of CAL. This reaction is industrially desired to hydrogenate the C=O bond to yield crotyl alcohol (COL), but the hydrogenation of the conjugated C=C bond, producing butanal (BAL), is thermodynamically favorable (Figure 2E). Kinetically, it shows the activity-selectivity trade-off, i.e., high selectivity can be achieved only at low activity.[2] On the Pt/Fe_3O_4 catalyst, the conversion of CAL was 4% (Figure 2F), and the selectivity of COL was approximately 50% (Figure 2G). This meant that the Pt/Fe_3O_4 catalyst performed similarly to conventional Pt nanoparticles, where the hydrogenation of the C=O bond proceeded competitively with that of the C=C bond.[30,31] By sharp contrast, the Pt/Fe catalyst featured a substantial improvement in both activity and selectivity; the conversion of CAL jumped to 40% (Figure 2F), whereas the selectivity toward COL approached 88% (Figure 2G). The superior performance of the Pt/Fe catalyst was further verified by the exceptionally high COL selectivity across a wide range of CAL conversion. When CAL conversion increased from 4% to 96%, the selectivity of COL declined only slightly from 93% to 83% (Figures S6A and S6B). Moreover, a stability test of the Pt/Fe catalyst for 100 h on stream at 353 K showed that the COL selectivity remained at around 90%, whereas the conversion of CAL stabilized at about 40% (Figure S6C). On the Pt/Fe_3O_4 catalyst, however, COL selectivity dropped sharply from 55% to 29% when CAL conversion increased from 4% to 33% (Figure S6D). The production rate of COL on the Pt/Fe catalyst, measured under a differential reactor condition, reached a value as high as 1.5 × 10^{-1} mmol·g_{Pt}^{-1}·s^{-1} at 353 K, exceeding that of the Pt/Fe_3O_4 catalyst (4.3 × 10^{-3} mmol·g_{Pt}^{-1}·s^{-1}) by 35-fold. Of note, this Pt-mass-based activity is 2–30 times greater than those of the state-of-the-art noble-metal catalysts with COL selectivity above

Please cite this article in press as: Zhou et al., Fine-tuned coordination environment of Pt-Fe-Pt active site for selective heterogeneous hydrogenation of crotonaldehyde, Chem (2024), https://doi.org/10.1016/j.chempr.2024.11.018

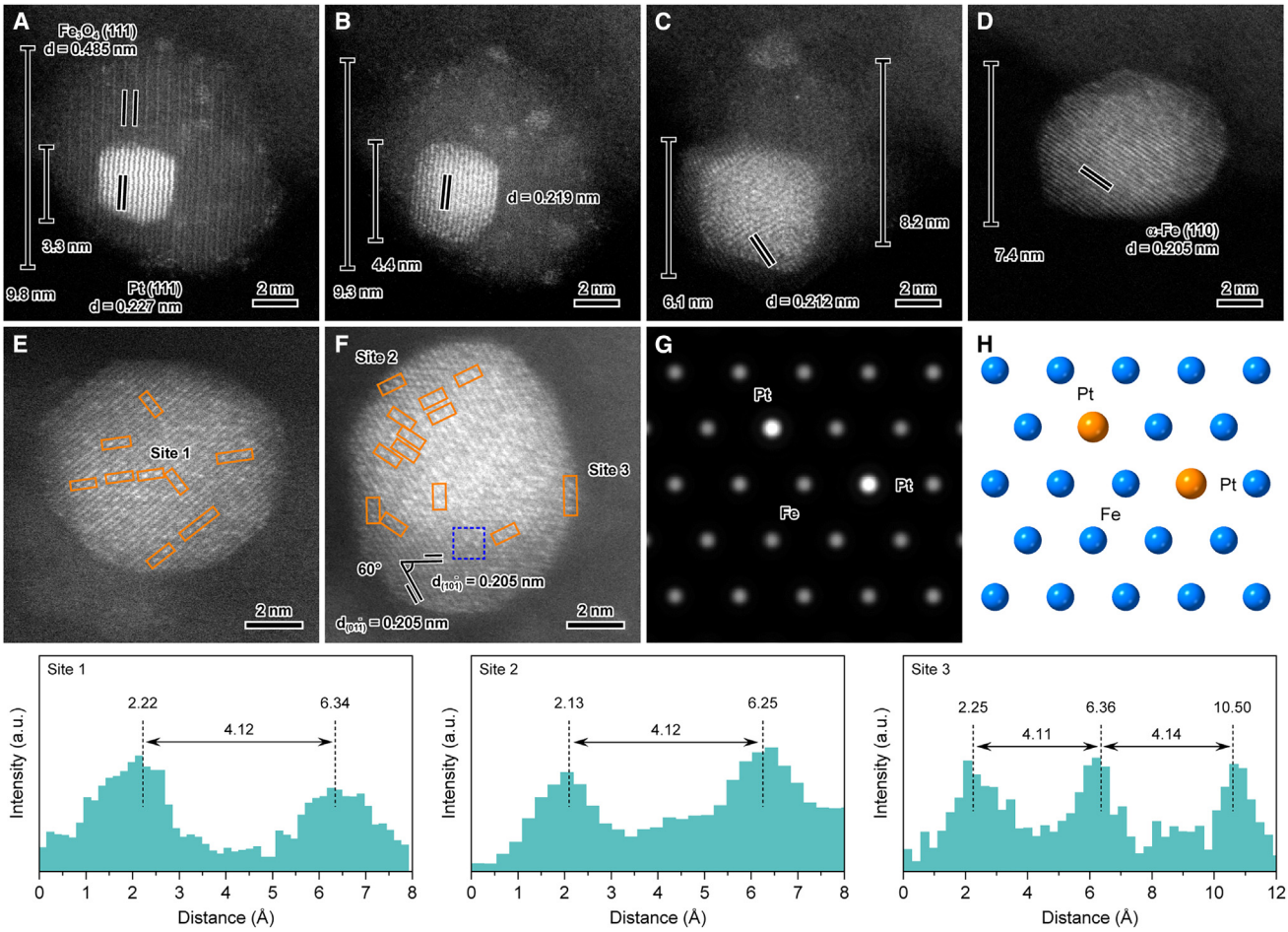

Figure 3. Environmental STEM observations on H_2 reduction of the Pt-Fe_2O_3 particle pair

(A–D) ESTEM images of a Pt–Fe_2O_3 particle pair under H_2 (0.1 mbar) at 473 K for 30 min (A), 673 K for 30 min (B), 873 K for 60 min (C), and 1,073 K for 20 min (D). Note that the indicated temperature for reducing Fe_2O_3 to α-Fe in the Pt-Fe_2O_3 particle pair in these ESTEM experiments is higher than that for preparing the Pt/Fe catalyst because the H_2 pressure (0.1 mbar) technically allowed by the electron microscope is much lower. Nevertheless, the reduction potential of the ESTEM (1,073 K, 0.1 mbar H_2) is roughly equivalent to that for preparing the Pt/Fe catalyst by treating the Pt-Fe_2O_3 particle pair with 1 bar H_2 at 673 K (Figure S7M).

(E and F) ESTEM images of Pt/Fe particles formed after exposure of the Pt-Fe_2O_3 particle pairs to H_2 at 1,073 K for 30 min (E) and 60 min (F). Pt-Fe-Pt heterotrimers are highlighted by the orange rectangles. The line-intensity profiles show the measured distances between two Pt atoms at sites 1–3.

(G and H) A simulated image (G) and the atomic arrangement (H) for the blue square region in (F).

80% (Table S1). All of these reaction data collectively demonstrated that the Pt/Fe catalyst was highly active and selective for hydrogenating the C=O bond in CAL, circumventing the commonly found activity-selectivity trade-offs in selective heterogeneous hydrogenation reactions.[2,30,31] Because the two catalysts were obtained by H_2 reduction of a same precursor, i.e., the Pt-Fe_2O_3 particle pair but merely at different temperatures (473 vs. 673 K), we inferred that the concurrently enhanced activity and selectivity on the Pt/Fe catalyst should originate from the geometric and electronic structure of the isolated Pt atoms on the α-Fe particle, as evidenced by the XAS data.

Dispersion of Pt particles into Pt-Fe-Pt heterotrimers

To conclusively identify the arrangement of Pt atoms in the Pt/Fe catalyst, we performed ESTEM experiments to track the structural evolution of the Pt-Fe_2O_3 particle pair upon heating to elevated temperatures under H_2 (0.1 mbar), during which the reduction of Fe_2O_3 to α-Fe induced dispersion of Pt particle into isolated Pt atoms. When a Pt-Fe_2O_3 particle pair was exposed to H_2 at 473 K, Fe_2O_3 was reduced into Fe_3O_4, and a particle-pair configuration where a 3.3 nm Pt particle sat on a 9.8 nm Fe_3O_4 particle was clearly resolved in the ESTEM image (Figure 3A). The lattice spacing of 0.485 nm indicated Fe_3O_4(111), whereas the lattice fringe of 0.227 nm referred to Pt(111). When the particle pair was heated to 673 K, the Fe_3O_4 particle shrank to 9.3 nm, whereas the Pt particle started to wet over it; the Pt(111) lattice spacing shortened to 0.219 nm as a result of the incorporation of smaller Fe atoms into the Pt lattice (Figure 3B). At 873 K, the Fe_3O_4 particle contracted to 8.2 nm, whereas the Pt particle expanded to 6.1 nm as the lattice spacing further narrowed to 0.212 nm (Figure 3C). At 1,073 K, an Fe particle of 7.4 nm formed with a lattice spacing of 0.205 nm for

Please cite this article in press as: Zhou et al., Fine-tuned coordination environment of Pt-Fe-Pt active site for selective heterogeneous hydrogenation of crotonaldehyde, Chem (2024), https://doi.org/10.1016/j.chempr.2024.11.018

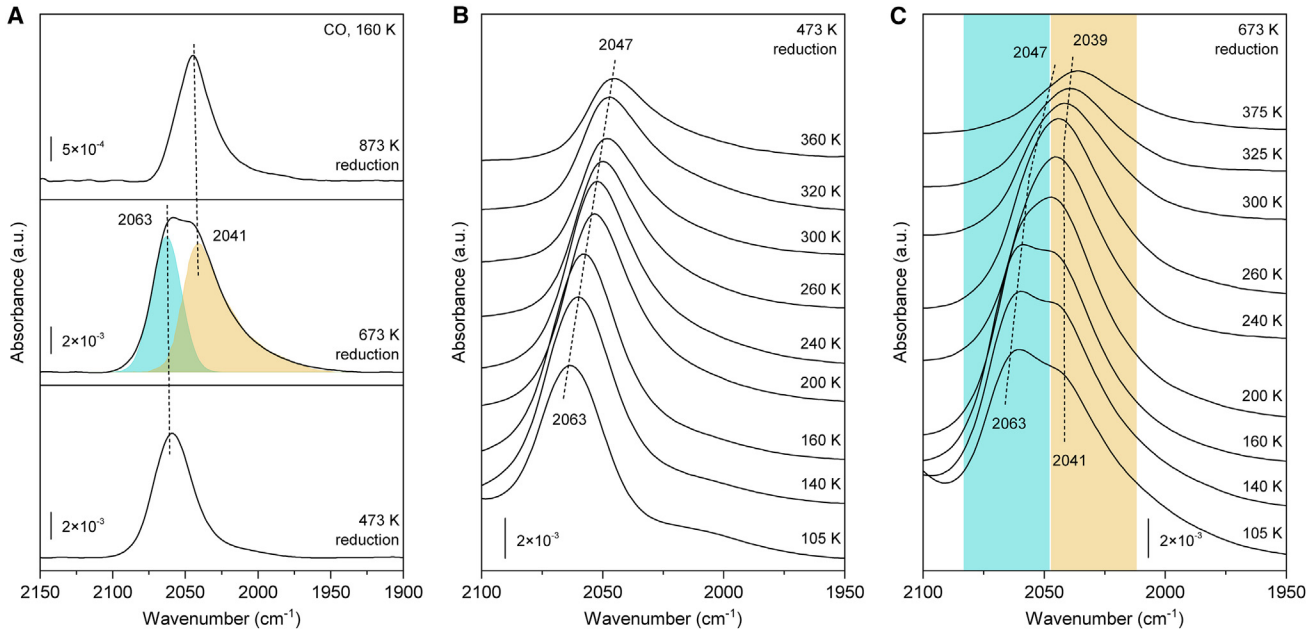

Figure 4. IR spectroscopic identification of the Pt-Fe-Pt heterotrimer

(A) *In situ* IR spectra recorded after the samples were exposed to CO (0.01 mbar) at 160 K. The samples were the result of treating the Pt-Fe_2O_3 particle pair with atomic hydrogen (5×10^{-5} mbar) at 473–873 K for 30 min. Here, the pre-reduction temperature (873 K) for achieving the fully isolated Pt atoms is slightly higher than that for preparing the Pt/Fe catalyst because of the much lower pressure of atomic H adopted by the ultrahigh vacuum FTIR spectroscopy system.
(B and C) Temperature-dependent IR spectra of the representative samples. The spectra were recorded after CO adsorption (0.01 mbar) at 105 K and subsequent annealing to the indicated temperatures.

α-Fe(110), over which isolated Pt atoms densely populated, as indicated by the bright dots (Figure 3D). ESTEM observations for a series of Pt-Fe_2O_3 particle pairs, in conjunction with EDX element mappings, consistently supported that the formation of α-Fe particle dispersed the Pt particle into isolated Pt atoms (Figure S7).

Electron energy loss spectroscopy (EELS) further elucidated the incorporation of Fe atoms into the Pt lattice during the dispersion of the Pt particle (Figure S8). Fe signals were detected only on Fe_3O_4 at 473 K, whereas weak Fe signals appeared at 673 K on the Pt particle when it started to wet on Fe_3O_4. The intensifying Fe signals on the disintegrating Pt particle at 873 K implicated that more Fe atoms incorporated into the Pt lattice. At 1,073 K, Fe was detected to cross the entire particle. Detailed analysis on the location of Pt atoms over the α-Fe particle found that they populated orderly in the form of the Pt-Fe-Pt heterotrimer. Line-intensity profiles of the indicated Pt-Fe-Pt heterotrimers (sites 1–3) showed a spatial separation of 0.41 nm between the two Pt atoms (Figures 3E and 3F). Image simulation found that the two Pt atoms substituted the Fe atoms in the α-Fe lattice and coordinated to the nearby Fe atoms, forming a Pt-Fe-Pt heterotrimer (Figures 3G and 3H).

In situ IR experiments using CO as the probe molecule provided spectroscopic evidence for the formation of the Pt-Fe-Pt heterotrimer. The Pt-Fe_2O_3 particle pair was first reduced with atomic hydrogen (5×10^{-5} mbar) at 473–873 K for 30 min, and the IR spectra of CO adsorption were then recorded (Figure 4A). On the sample pre-reduced at 473 K, the IR spectrum exhibited a single band at 2,063 cm^{-1}, which is typical for CO bound to high-coordinated Pt sites exposed by the Pt particle.[32] When the pre-reduction temperature was raised to 673 K, an intense low-lying band at 2,041 cm^{-1} emerged, which is characteristic of CO adsorbed on highly diluted Pt sites. Over the sample pre-treated by atomic hydrogen at 873 K, the high-lying band at 2,063 cm^{-1} disappeared, whereas the low-lying band at 2,041 cm^{-1} remained unchanged in frequency, referring to the highly dispersed Pt sites. Temperature-dependent IR spectra detailed the coordination environments of these Pt entities (Figures 4B and 4C). A coverage-induced, 16 cm^{-1} frequency red shift was observed for the 2,063 cm^{-1} band when the sample was heated from 105 to 360 K, i.e., CO desorption. This large frequency shift stemmed from the strong dipole-dipole coupling between CO molecules bound to the neighboring highly coordinated Pt sites over the Pt particle.[33] By contrast, the 2,041 cm^{-1} band exhibited a much smaller red shift of only 2 cm^{-1}, validating the atomically dispersed Pt. A closer inspection of the IR data revealed the strong electronic interaction between the Pt and Fe atoms in the Pt-Fe-Pt heterotrimer. The band at 2,041 cm^{-1}, characteristic of CO bound to the isolated Pt sites, was much lower in frequency than those reported for CO adsorbed on Pt SAAs, typically Pt_1Cu (2,088–2,112 cm^{-1}),[11,34–36] demonstrating the enhanced electron back donation from the Pt 5d band to the CO 2π* orbital.[37] Instead, it was close to those measured for CO adsorbed on the isolated Pt atoms in intermetallics, e.g., PtGa (2,050 cm^{-1})[38] and PtZn (2,047 cm^{-1}).[39] This suggested that the Pt atoms in the Pt-Fe-Pt heterotrimer coordinated to α-Fe through intermetallic bonds, in line with the EXAFS data (Figures 2B and 2C) and ESTEM observations (Figures 3E–3H).

Please cite this article in press as: Zhou et al., Fine-tuned coordination environment of Pt-Fe-Pt active site for selective heterogeneous hydrogenation of crotonaldehyde, Chem (2024), https://doi.org/10.1016/j.chempr.2024.11.018

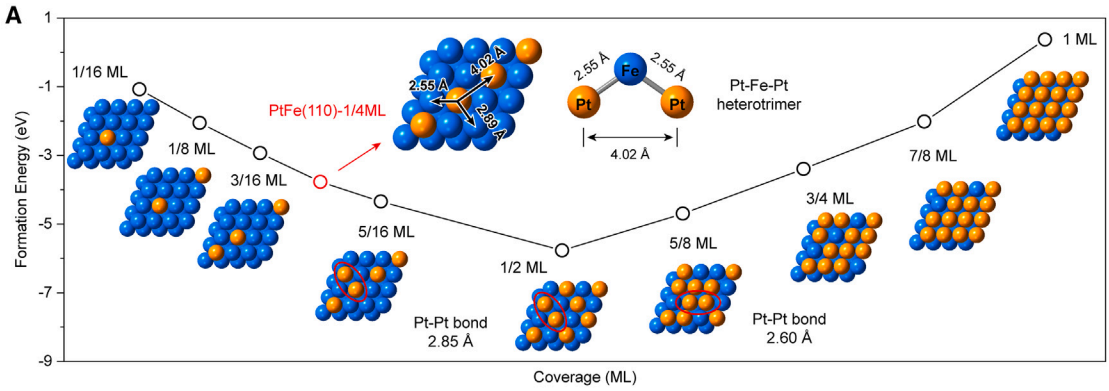

B DFT calculations for CO adsorption on PtFe(110)-1/4ML

System	E_{ads}(CO) / eV	R_{C-O} / Å	R_{Pt-C} / Å	Q / |e|	ω_e / cm^{-1}	Structure
PtFe(110)-1/4ML-A	-1.37	1.162	1.908	-0.12	2043	
PtFe(110)-1/4ML-B	-1.53	1.158	1.925	-0.14	2043	
PtFe(110)-1/4ML-C	-1.47	1.161	1.916	-0.11	2047	

E_{ads}, CO adsorption energy; R_{C-O}, C-O bond length; R_{Pt-C}, C-Pt distance; Q, CO Bader charge; ω_e, CO stretch frequency.

Figure 5. DFT calculations on Pt-doped α-Fe(110)

(A) Optimized structures and formation energies at the indicated Pt coverages.

(B) Vibrational frequencies for the on-top CO–Pt band. The adsorbed CO is shown by the red (O) and gray (C) spheres.

Catalysis by the Pt-Fe-Pt heterotrimer

To elaborate the geometric and electronic structure of the Pt-Fe-Pt heterotrimer, we performed DFT calculations on the coordination environment of Pt atoms on α-Fe(110). The result suggested that substituting surface Fe on α-Fe(110) by Pt up to 1/2 monolayer (ML) was exothermic, whereas the formation energy was monotonously downhill to −5.77 eV (Figure 5A). At 1/4 ML Pt coverage (labeled as PtFe(110)-1/4ML), Pt atoms coordinated to Fe atoms with bond lengths of 2.55 and 2.89 Å, forming a Pt-Fe-Pt configuration with a spatial distance of 4.02 Å between the two Pt atoms. When Pt coverage was increased to 1/2 ML, however, an additional Pt–Pt bond with a length of 2.85 Å emerged. We then used this DFT-simulated model to quantify the location of Pt atoms in the Pt/Fe catalyst. Taking the size of the Pt/Fe particle (8.6 nm) determined from ESTEM images and assuming that all Pt atoms were located on the top layer of the α-Fe particle, we estimated the maximum Pt coverage to be 0.307 ML (Figure S9). This is slightly higher than that of PtFe(110)-1/4ML but much lower than that of 1/2 ML Pt on α-Fe(110). Because the EXAFS spectrum of the Pt/Fe catalyst did not show Pt–Pt bonds but the Pt–Fe_1 and Pt–Fe_2 bonds agreed well with those in PtFe (110)-1/4ML, we inferred that the Pt atoms in the Pt/Fe catalyst were more analogous to those in PtFe(110)-1/4ML. However, any extra Pt atoms might diffuse into the subsurface of the α-Fe particle. This was further supported by the close vibrational frequencies of CO bound to the Pt-Fe-Pt heterotrimer in the IR experiments (2,041 cm^{-1}, Figure 4A) and the DFT-calculated values (2,043–2,047 cm^{-1}) on PtFe(110)-1/4ML (Figure 5B).

To identify the origin of the simultaneously promoted activity and selectivity of the Pt/Fe catalyst for hydrogenating the C=O bond in CAL, we analyzed the potential energy surfaces (PESs) via DFT calculations on PtFe(110)-1/4ML, a model representing the Pt/Fe catalyst. For comparison, we first estimated the PESs on Pt(111) and α-Fe(110) and found that neither surface was suitable for a selective hydrogenation of the C=O bond as a result of the unfavorable thermodynamics and/or kinetics (Figure S10). Over PtFe(110)-1/4ML, preferential hydrogenation of the C=O bond became feasible because the electron transfer from Fe to Pt generated electron-enriched (Pt) and electron-deficient (Fe) sites in the Pt-Fe-Pt heterotrimer. Density-of-states profiles (Figures S11A–S11C) revealed that the hybridization of Fe 3d with Pt 5d altered the d valence states of Fe and Pt. The d-band center of Fe upshifted to a higher energy than that on α-Fe(110), indicating the positively charged character, whereas the d-band center of Pt downshifted to a lower energy than that of Pt(111), showing the electron-enriched feature. Bader charges analysis (Figure S11D) indicated a charge implement (−0.79 *e*) by the Pt atom but a charge depletion (+0.11 *e*) by the Fe atom. Two-dimensional electron localization functions (Figure S11E) suggested that electrons were highly localized between Pt and Fe atoms. This strong electronic interaction between Pt and Fe in the Pt-Fe-Pt heterotrimer is in line with the IR data, where the low-frequency band at 2,041 cm^{-1} is

characteristic of CO bound to the isolated Pt sites coordinating to α-Fe in intermetallic bonds. The high electron density of the Pt atom weakened the adsorption of the C=C bond, whereas the electrophilic Fe atom favorably adsorbed and activated the C=O bond.[37,40] As a result, CAL adsorption was enhanced while COL desorption was facilitated, enabling a preferential hydrogenation of the C=O bond. *In situ* IR spectra of the CAL and COL adsorptions on the Pt/Fe catalyst experimentally verified a stronger adsorption of CAL but a weaker adsorption of COL (Figures S12A and S12B). In addition, IR spectra recorded under the reaction conditions over time convincingly showed selective hydrogenation of the C=O bond (Figure S12C). Mechanistic studies using *in situ* sum-frequency generation vibrational spectroscopy identified a unique reaction pathway for selectively producing COL: involving CAL adsorption via the aldehyde oxygen atom to the catalyst surface.[41]

Specifically, CAL adsorbed in a η^4-π(CC)-π(CO) mode such that the left-end Pt atom anchored the C=C bond and the central Fe atom captured the C=O group (Figure 6A). This site-bond configuration had an adsorption energy as strong as −1.68 eV (Figure 6B) and hence stabilized the two functional groups in CAL. On the other hand, COL, the desired product, adsorbed in a η^3-π(CC)-σ(O) mode such that the O atom linked to the Fe atom, whereas the C=C group π-bonded to the left-end Pt atom. This resulted in an adsorption energy of −1.20 eV and reversibly facilitated the desorption of COL. Bader charges of adsorbates suggested that the enhanced adsorption of CAL resulted from accepting electrons from the electron-enriched Pt atom, whereas the weakened adsorption of COL originated from accepting electrons from the electron-deficient Fe atom but donating electrons to the electron-enriched Pt atom (Figure 6C). Kinetically, the Pt-Fe-Pt heterotrimer accelerated hydrogenation of the C=O bond by lowering the energy barriers for the sequential addition of two H atoms (Figures 6D and 6E). In the first step, the H atom captured by the right-end Pt atom, with a Bader charge of +0.28 *e* (TS1), interacted with the O atom in C=O on the Fe atom and formed a mono-hydrogenated intermediate with an energy barrier of 1.43 eV (TS1). Then, the second H atom was added to the intermediate with an even lower energy barrier (0.76 eV, TS2). By contrast, the energy barriers for hydrogenating the C=C bond became larger, 1.62 eV for adding the first H atom and 1.10 eV for the second one. Altogether, the coordination environment of the Pt-Fe-Pt active site, fine-tuned by the interaction between Pt and Fe atoms, enabled a thermodynamically preferential adsorption and a kinetically favorable activation of the C=O bond in CAL. This resulted in the simultaneously enhanced activity and selectivity for CAL hydrogenation on the Pt/Fe catalyst.

DISCUSSION

The Pt-Fe-Pt heterotrimer in the Pt/Fe catalyst stemmed from the surface framework provided by the α-Fe particle. H_2 reduction of FeO_x-supported Pt particles is usually done for investigating the strong metal-support interactions.[42] H_2 facilely dissociates into H atoms on Pt, but FeO_x is hardly reduced to α-Fe at temperatures below 673 K because the activated H atoms combine and desorb as molecular H_2 during the long-distance transportation over the oxide supports.[43–45] Here, the Pt-Fe_2O_3 particle-pair geometry greatly facilitated the reduction of Fe_2O_3 to α-Fe at 673 K in fabricating the Pt/Fe catalyst. The 3.3 nm Pt particle epitaxially grew on the Fe_2O_3 particle of 9.8 nm, and this Pt-Fe_2O_3 proximity shortened the diffusion length for the activated H atoms from Pt to Fe_2O_3 to less than 10 nm (Figures 1A–1C, S1G, and S1H). Once Fe atoms formed locally, they migrated toward and diffused into the Pt lattice as a result of the much higher diffusion coefficient of Fe in Pt, which is 500 times greater than that of Pt in Fe at 600 K.[46] This was evidenced by the shrinking lattice spacing of Pt(111) in the ESTEM images (Figures 3A–3D) and the intensifying Fe EELS signals on the disintegrating Pt particle (Figure S8). Subsequently, the formation of Pt–Fe bonds drove the dispersion and relocation of Pt atoms, as theoretically justified by the greater bond energy for Pt–Fe (2.18 eV/atom) than for Fe–Fe (1.60 eV/atom) and Pt–Pt (1.95 eV/atom)[47] and experimentally verified by the IR data (Figure 4). In short, the reduction of Fe_2O_3 to α-Fe by H_2 at 673 K dispersed the Pt particle into isolated Pt atoms in the form of a Pt-Fe-Pt heterotrimer on the newly formed α-Fe particle in the Pt/Fe catalyst. This offers a strategy for tailoring active sites on bimetallic catalysts with atomic precision.

The Pt-Fe-Pt active site, thus created by the coupling of two Pt atoms with a central Fe atom on the α-Fe particle, accounted for the unparalleled efficiency in CAL hydrogenation. The Pt and Fe atoms acted in a targeted but synergistic manner upon interacting with the reacting molecules. The left-end Pt atom stabilized the C=C bond, the bridging Fe atom activated the C=O bond, and the right-end Pt atom supplied H atoms to hydrogenate the C=O bond on Fe while keeping the C=C bond on the left-end Pt atom intact. This quantifies a site-bond recognition pattern in selective heterogeneous hydrogenation, which is closely related to the geometric and electronic interactions between the metal atoms in the active site and the target functional groups in the reacting molecule. A control experiment further identified the crucial role of the Pt-Fe-Pt active site in selectively hydrogenating the C=O bond in CAL. The Pt-Fe_2O_3 particle pair was treated with H_2 at a higher temperature, 873 K. The resulting sample (Pt/Fe-R) still featured isolated Pt atoms, but most of them diffused into the subsurface of the α-Fe particle (Figure S13). Reaction testing for CAL hydrogenation showed that the conversion of CAL dropped to 8.6%, but the selectivity toward COL (92.7%) stayed at the same level as the Pt/Fe catalyst (Figure S14). This meant that the Pt-Fe-Pt active site, remaining on the sample surface, catalyzed the hydrogenation of the C=O bond preferentially.

More broadly, the active site that is directly involved in a catalytic cycle should be a highly local area, i.e., only a few atoms interact with the reacting molecules for a chemical reaction to occur.[3] In this scenario, the matching between the active site and the reacting molecules, in terms of their geometric and electronic configurations, would dominate catalysis intrinsically. In addition to the frequently addressed electronic interaction, the geometric interaction plays a crucial role in directing the reaction route. An early surface science study clearly demonstrated that precisely spacing Pd monomers on Au single crystals yielded active and selective catalytic sites for the synthesis of vinyl acetate.[48] Pd atoms at a distance of 0.408 nm, regulated by the

Please cite this article in press as: Zhou et al., Fine-tuned coordination environment of Pt-Fe-Pt active site for selective heterogeneous hydrogenation of crotonaldehyde, Chem (2024), https://doi.org/10.1016/j.chempr.2024.11.018

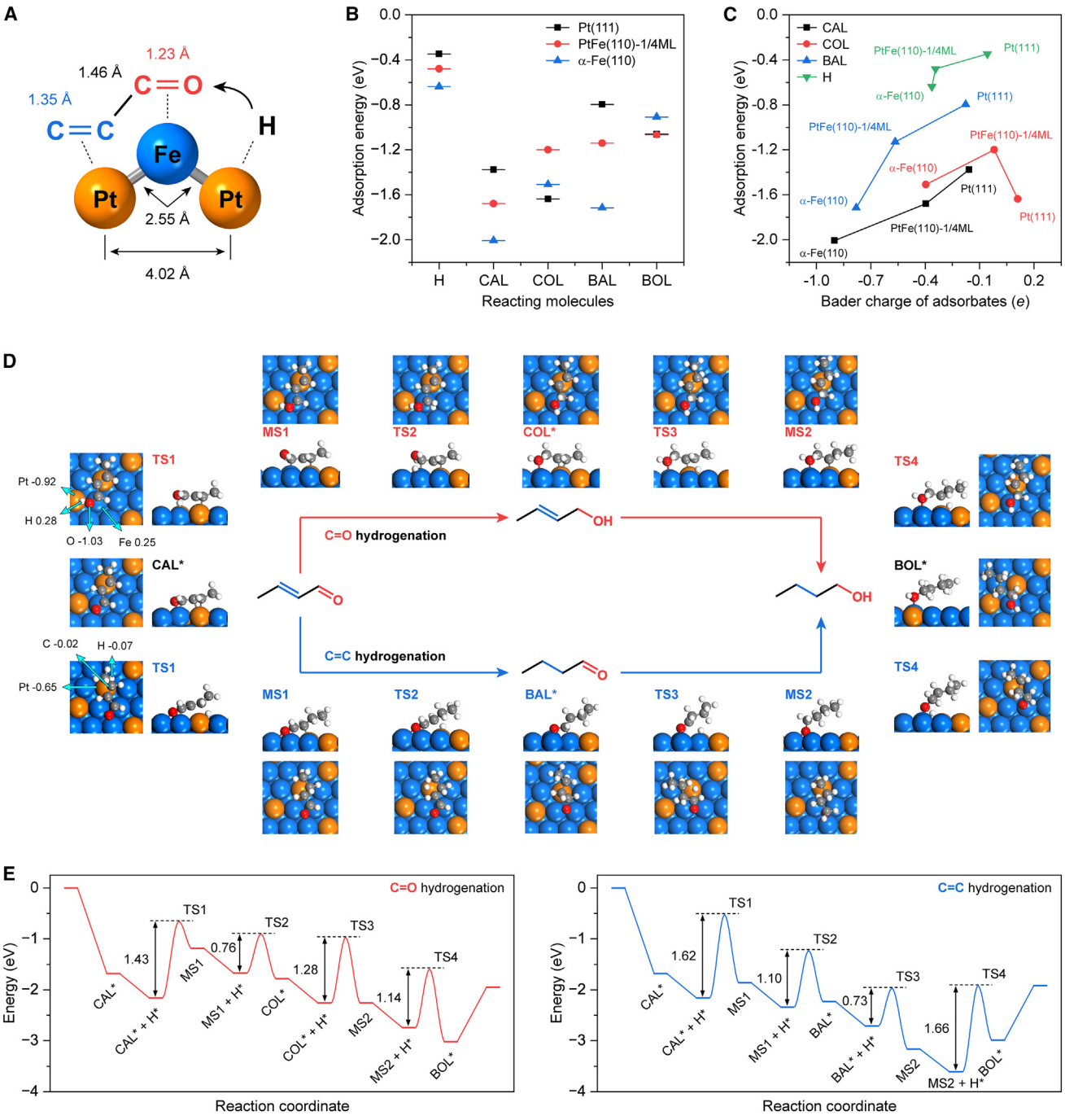

Figure 6. Theoretical insights into Pt-Fe-Pt catalysis

(A) CAL adsorption and activation. The terminal methyl group and H atoms in CAL are intentionally hidden for simplification.

(B) Adsorption energies of the molecules.

(C) Bader charges of the adsorbates.

(D and E) Reaction routes (D) and energy profiles (E) for hydrogenating the C=O and C=C bonds. The Bader charges (with unit *e*) of the corresponding atoms in TS1 are indicated in (D).

surface interatomic spacing of Au(100), geometrically allowed the coupling of surface ethylenic and acetate species. But Pd atoms on Au(111) were too far (0.499 nm) to catalyze the coupling reaction. A more recent study combining experimental investigations and theoretical calculations found that Pd-M-Pd (M = Cu, Au, and Ag) ensembles derived from Pd–Zn

intermetallic compounds were catalytically distinct from Pd single atoms and timers.[7] The central M atom, bridging the two Pd atoms, decisively controlled the catalysis for the selective hydrogenation of acetylene to ethylene. Here, the spatial distance (0.41 nm) between the two Pt atoms in the Pt-Fe-Pt active site geometrically allowed a flexible adsorption of the CAL molecule, through which the C=O bond was selectively hydrogenated against the C=C bond. This finding provides in-depth insights for understanding surface catalytic reaction at atomic and molecular levels, and we foresee its applicability to a wide range of bimetallic catalysts that are industrially used for the production of fine and specialty chemicals.

METHODS

Catalyst preparation

The Pt-Fe_3O_4 particle pair was prepared via a two-step procedure: the initial synthesis of the PtFe seed and the subsequent growth of Fe_3O_4 particle around it. A mixture containing platinum acetylacetonate (0.0183 g), iron stearate (0.0195 g), myristic acid (0.22 g), n-octadecylamine (1 g), and n-octadecane (20 mL) was heated to 393 K and stirred for 20 min under N_2 flow. It was further heated to 583 K and kept there for 35 min, yielding the PtFe seed with a Pt/Fe molar ratio of 2/1. After it cooled down to 353 K, iron stearate (0.6 g) and 1,2-dodecanediol (0.3 g) were added into the suspension. The mixture was first heated at 393 K for 30 min and then at 583 K for 35 min, forming the Pt-Fe_3O_4 particle pair. After cooling down to 353 K, the Pt-Fe_3O_4 particle pair was precipitated by the addition of 85 mL ethanol and 10 mL isopropanol into the solution. The solid was then collected by centrifugation; washed with a mixture of methanol, isopropanol, and hexane; and dispersed into 200 mL hexane (0.23 $mmol_{Pt}\cdot L^{-1}$).

The Pt-Fe_3O_4 particle pair was deposited onto a high-surface-area SiO_2 (400 $m^2\cdot g^{-1}$) support by a colloid-deposition method. 200 mL Pt-Fe_3O_4 particle pair (0.23 $mmol_{Pt}\cdot L^{-1}$ in hexane) was added dropwise to a suspension of 0.89 g SiO_2 in 200 mL hexane, and the mixture was stirred for 15 min at room temperature. The precipitate was collected by centrifugation, washed with hexane, dried at 353 K overnight under vacuum, and finally calcined at 873 K in air for 4 h. The sample thus obtained was labeled as the Pt-Fe_2O_3 particle pair. Elemental analysis, performed via inductively coupled plasma atomic emission spectroscopy (ICPS-8100 spectrometer), identified that the contents of Pt and Fe were 0.9 and 4.2 wt % (a total metal loading of 5.1 wt %), respectively, equaling a Pt/Fe molar ratio of 1/16.

The Pt/Fe_3O_4 and Pt/Fe catalysts were obtained from a reduction of the Pt-Fe_2O_3 particle pair with H_2 at 473 and 673 K for 2 h, respectively.

Catalyst characterization

H_2-TPR

Temperature-programmed reduction by hydrogen (H_2-TPR) of the Pt-Fe_2O_3 particle pair was done on an AutoChem II 2920 instrument (Micromeritics). A 150 mg Pt-Fe_2O_3 particle pair (40–60 mesh) was loaded into a U-type quartz tubular reactor, pretreated with a 20 vol % O_2/Ar mixture (30 $mL\cdot min^{-1}$) at 673 K for 1 h, and purged with Ar (30 $mL\cdot min^{-1}$) at the same temperature for 30 min. After cooling down to 223 K under Ar flow (30 $mL\cdot min^{-1}$), the sample was exposed to a 10 vol % H_2/Ar mixture (30 $mL\cdot min^{-1}$) and then heated to 1,173 K at a rate of 5 $K\cdot min^{-1}$. The amount of hydrogen consumed was analyzed with a thermal conductivity detector.

XRD

Powder XRD patterns were recorded over a Rigaku D/MAX-2500/PC diffractometer with a Cu K_α radiation source operated at 40 kV and 200 mA. *In situ* XRD experiments were done in a high-temperature chamber with the same diffractometer. A 180 mg Pt-Fe_2O_3 particle pair was pressed into a self-supporting wafer and mounted in the chamber. The sample was heated from room temperature to 873 K at a rate of 10 $K\cdot min^{-1}$ under H_2 flow (30 $mL\cdot min^{-1}$) and kept at the desired temperatures for 75 min, during which XRD patterns were collected at a scanning speed of 1° per minute.

XPS

X-ray photoelectron spectra (XPS) were collected on an ESCALAB 250Xi instrument (ThermoFisher) with an Al K_α radiation source operated at 15 kV and 10.8 mA. The Pt-Fe_2O_3 particle pair was pressed into a thin disc and mounted on a sample holder placed in the pre-treatment chamber, where it was reduced with H_2 (100 $mL\cdot min^{-1}$) at 473–773 K for 2 h. After cooling down to 373 K, the sample was transferred to the analysis chamber, where it was further cooled down to room temperature and subjected to spectra collection of Pt 4f, Fe 2p, and Si 2p. The charging effect was corrected via adjustment of the binding energy of Si 2p to 103.6 eV.

XAS

X-ray absorption spectra (XAS) at the Pt L_3-edge (11,564.0 eV) and Fe K-edge (7,112.0 eV), including XANES and EXAFS, were taken at the BL14W1 beamline of the Shanghai Synchrotron Radiation Facility of China. The storage ring was operated at 3.5 GeV with a current of 200 mA. The X-ray was monochromatized by a Si (111) double-crystal monochromator. A 70 mg Pt-Fe_2O_3 particle pair was pressed into a self-supporting wafer and mounted into a reaction cell, where it was treated with H_2 (50 $mL\cdot min^{-1}$) at 473 or 673 K for 2 h. The spectra were recorded at room temperature in the transmission mode with ion chambers as the detector. The data were processed according to standard procedures with the Athena and Artemis modules of the IFEFFIT software packages.[49] EXAFS contributions from different coordination shells were estimated with a hanning window (dk = 1.0 $Å^{-1}$). Quantitative curve-fittings were done in the R-space (Fe = 1.0–3.6 Å; Pt = 1.4–3.1 Å) with a Fourier transform k-space range (Fe = 3.1–13.6 $Å^{-1}$; Pt = 3.0–13.2 $Å^{-1}$). The overall amplitude reduction factor, S_0^2, was set to 0.9 for the Pt L_3-edge and 0.8 for the Fe K-edge. Pt foil, PtO_2, Fe foil, Fe_3O_4, and Fe_2O_3 were used as the references.

STEM and ESTEM

Aberration-corrected HAADF-STEM images were acquired over a Hitachi HF5000 microscope at 200 kV. The specimen was prepared via ultrasonic dispersion of the powder sample into ethanol, deposition of droplets of the suspension onto a lacey carbon-coated copper grid, and air drying. ESTEM experiments were performed on the same microscope. A microelectromechanical-system-based heating holder and a four-electrode SiN_x chip were used to control the temperature. H_2 was

Please cite this article in press as: Zhou et al., Fine-tuned coordination environment of Pt-Fe-Pt active site for selective heterogeneous hydrogenation of crotonaldehyde, Chem (2024), https://doi.org/10.1016/j.chempr.2024.11.018

introduced to the sample by a nozzle installed in the column of the microscope. The Pt-Fe_2O_3 particle pair was mounted onto the chip and heated up to 1,073 K under H_2 (around 0.1 mbar). A low-dose rate was adopted for image collection, and the sample was exposed to the electron beam only during image acquisition.

IR

IR spectra of CO adsorption were recorded on a Fourier transform IR (FTIR) spectrometer (Bruker Vertex 80v) combined with a multi-chamber ultrahigh vacuum system (Prevac).[50] A 200 mg Pt-Fe_2O_3 particle pair was pressed into an inert metal mesh, mounted onto a sample holder, and reduced by atomic hydrogen (5×10^{-5} mbar) at 473–873 K for 30 min. Exposure to CO was done with a leak-valve-based directional doser connected to a tube (inner diameter = 2 mm) that terminated 3 cm from the sample. Before each exposure, a spectrum of the clean sample was recorded as the background reference. For the temperature-programmed analysis, the sample was first exposed to 0.01 mbar CO at 105 K and then heated to higher temperatures at a rate of 0.05 K·s^{-1}. IR data were collected from 1,024 scans with a resolution of 4 cm^{-1}. Peak fittings on the spectra for CO adsorbed at Pt-related sites were performed by the Gaussian function.

Computational details

The Vienna *ab initio* Simulation Package (VASP)[51,52] was employed for the spin-polarized periodic DFT calculations with the PBE-vdW exchange-correlation functional.[53] The projector-augmented wave (PAW) method was used for describing the core electron interactions.[54] A plane wave basis set with a 400 eV cutoff energy was used, and the convergence threshold for electronic self-consistent interactions was 10^{-5} eV. A spin polarization was included for iron systems to correctly account for the magnetic properties. The structure optimization and transition-state search were converged to the extent that the maximum residual forces were 0.02 and 0.05 eV/Å, respectively, in all relaxed degrees of freedom. Transition states were determined by the climbing image nudged elastic band (CI-NEB) method[55,56] and the improved dimer method[57] and were verified to possess only one vibrational mode with a negative curvature in the direction of the bond-breaking or bond-making process.

Calculations on the bulk crystal structure of α-Fe (bcc) gave a lattice constant of 2.85 Å and a local spin magnetic moment of 2.189 μ_B, agreeing well with other DFT calculations.[58] The fcc-Pt bulk unit cell with an optimized lattice constant of 4.02 Å was consistent with the experimental value.[59] The models of $p(4 \times 4)$ supercell slabs with four atomic layers for α-Fe (110) and Pt (111) surfaces were used, and the top two layers including adsorbates were allowed to relax. A vacuum of more than 20 Å was applied to prevent the interaction between slabs. The surface Brillouin zone was sampled on a $(3 \times 3 \times 1)$ Monkhorst-Pack k-point grid.

The formation energy of $Pt_xFe(110)$ surface alloy was defined as follows:

$$E_f = E_{Pt_xFe(110)} + \frac{x}{2} E_{Fe\text{-}bulk} - E_{Fe(110)} - \frac{x}{4} E_{Pt\text{-}bulk},$$

where $E_{Pt_xFe(110)}$, $E_{Fe(110)}$, $E_{Fe\text{-}bulk}$, and $E_{Pt\text{-}bulk}$ are the total energies of $Pt_xFe(110)$ surface alloy, clean Fe (110) surface, bulk Fe, and bulk Pt, respectively; x is the number of Pt atoms on the $p(4 \times 4)$ supercell Fe (110) surface.

The adsorption energy was calculated by $\Delta E_{ads} = E_{tot} - E_{slab} - E_{gas}$, where E_{tot} and E_{slab} refer to the energy of the slab with adsorbates and the energy of clean slab, respectively, and E_{gas} represents the energy of involved gas-phase adsorbates in a neutral state. The reaction energy and the activation energy barrier were calculated as $\Delta E_{rxn} = E_{FS} - E_{IS}$ and $E_a = E_{TS} - E_{IS}$, respectively, where E_{IS}, E_{FS}, and E_{TS} refer to the energies of the initial state, the final state, and the transition state, respectively.

CO vibrational stretching frequencies were computed within the harmonic approximation, in which CO and its first neighboring atom were considered in the calculations. The gas-phase CO bond length (1.141 Å) and stretching frequency (2,119 cm^{-1}) were obtained at the PBE-vdW level. The scaling factor (2,170/2,119 = 1.0239) was applied to all frequencies to account for the difference with respect to the experimental CO frequency in the gas phase (2,170 cm^{-1}) reported in a previous work.[60]

Catalytic test

Hydrogenation of CAL on the Pt catalysts was conducted with a continuous-flow fixed-bed quartz tubular reactor (inner diameter = 10 mm) under atmospheric pressure. A 200 mg Pt-Fe_2O_3 particle pair (40–60 mesh) was placed between two layers of quartz wool inside the reactor and reduced with H_2 (30 mL·min^{-1}) at 473 or 673 K for 2 h. After cooling down to 353 K in H_2 flow (30 mL·min^{-1}), the catalyst was exposed to a 1 vol % CAL/99 vol % H_2 mixture, obtained when 50 mL·min^{-1} H_2 was passed through a bubbler containing CAL at 273 K. The reaction was tested for 12 h, and the effluent from the reactor was analyzed online by a gas chromatograph equipped with a flame ionization detector. For the kinetic evaluation, we adjusted the conversion of CAL to below 10% by adjusting the flow rate of the reaction gas and/or the mass of the catalyst, ensuring that the reaction rate was measured under a differential reactor condition.

RESOURCE AVAILABILITY

Lead contact

Requests for further information and resources should be directed to and will be fulfilled by the lead contact, Wenjie Shen (shen98@dicp.ac.cn).

Materials availability

This study did not generate new, unique reagents.

Data and code availability

The data that support the plots within this paper and other findings of this study are available from the corresponding authors upon reasonable request.

ACKNOWLEDGMENTS

This work was supported by the National Key R&D Program of China (2022YFA1604103, 2021YFA1502802, and 2023YFA1508500), the National Natural Science Foundation of China (21573221, 21533009, and 22221003), the Deutsche Forschungsgemeinschaft (DFG; 426888090–SFB1441), the Strategic Priority Research Program of the Chinese Academy of Sciences

(XDB0450102), and the Innovation Program for Quantum Science and Technology (2021ZD0303302). We thank Hiroaki Matsumoto and Chaobin Zeng at Hitachi High-Technologies Co., Ltd., for helping with the ESTEM experiments and the Supercomputing Center of the University of Science and Technology of China for DFT calculations.

AUTHOR CONTRIBUTIONS

D.Z., Y.L., and S.L. prepared materials, characterized structures, and conducted catalytic tests. J.W. and Y.W. performed IR experiments and data analysis. M.J. and W.-X.L. performed DFT calculations. Z.J. conducted XAS measurements and analyzed the data. Y.Z. and J.W. performed STEM experiments. C.W. provided suggestions on the experiments. Y.L., W.-X.L., Y.W., and W.S. designed the experiments and wrote the paper. All authors discussed the results and commented on the paper.

DECLARATION OF INTERESTS

The authors declare no competing interests.

SUPPLEMENTAL INFORMATION

Supplemental information can be found online at https://doi.org/10.1016/j.chempr.2024.11.018.

Received: June 5, 2024
Revised: November 10, 2024
Accepted: November 25, 2024
Published: January 3, 2025

REFERENCES

1. Zhang, L., Zhou, M., Wang, A., and Zhang, T. (2020). Selective hydrogenation over supported metal catalysts: from nanoparticles to single atoms. Chem. Rev. *120*, 683–733. https://doi.org/10.1021/acs.chemrev.9b00230.
2. Luneau, M., Lim, J.S., Patel, D.A., Sykes, E.C.H., Friend, C.M., and Sautet, P. (2020). Guidelines to achieving high selectivity for the hydrogenation of α,β-unsaturated aldehydes with bimetallic and dilute alloy catalysts: a review. Chem. Rev. *120*, 12834–12872. https://doi.org/10.1021/acs.chemrev.0c00582.
3. Liu, L., and Corma, A. (2023). Bimetallic sites for catalysis: from binuclear metal sites to bimetallic nanoclusters and nanoparticles. Chem. Rev. *123*, 4855–4933. https://doi.org/10.1021/acs.chemrev.2c00733.
4. Nakaya, Y., and Furukawa, S. (2023). Catalysis of alloys: classification, principles, and design for a variety of materials and reactions. Chem. Rev. *123*, 5859–5947. https://doi.org/10.1021/acs.chemrev.2c00356.
5. Mitchell, S., and Pérez-Ramírez, J. (2021). Atomically precise control in the design of low-nuclearity supported metal catalysts. Nat. Rev. Mater. *6*, 969–985. https://doi.org/10.1038/s41578-021-0036.
6. Peng, M., Dong, C., Gao, R., Xiao, D., Liu, H., and Ma, D. (2021). Fully exposed cluster catalyst (FECC): toward rich surface sites and full atom utilization efficiency. ACS Cent. Sci. *7*, 262–273. https://doi.org/10.1021/acscentsci.0c01486.
7. Dasgupta, A., He, H., Gong, R., Shang, S.-L., Zimmerer, E.K., Meyer, R.J., Liu, Z.-K., Janik, M.J., and Rioux, R.M. (2022). Atomic control of active-site ensembles in ordered alloys to enhance hydrogenation selectivity. Nat. Chem. *14*, 523–529. https://doi.org/10.1038/s41557-021-00855-3.
8. Gu, J., Xu, Y., and Lu, J. (2023). Atom-precise low-nuclearity cluster catalysis: opportunities and challenges. ACS Catal. *13*, 5609–5634. https://doi.org/10.1021/acscatal.3c01449.
9. Kyriakou, G., Boucher, M.B., Jewell, A.D., Lewis, E.A., Lawton, T.J., Baber, A.E., Tierney, H.L., Flytzani-Stephanopoulos, M., and Sykes, E.C.H. (2012). Isolated metal atom geometries as a strategy for selective heterogeneous hydrogenations. Science *335*, 1209–1212. https://doi.org/10.1126/science.1215864.
10. Darby, M.T., Stamatakis, M., Michaelides, A., and Sykes, E.C.H. (2018). Lonely atoms with special gifts: breaking linear scaling relationships in heterogeneous catalysis with single-atom alloys. J. Phys. Chem. Lett. *9*, 5636–5646. https://doi.org/10.1021/acs.jpclett.8b01888.
11. Hannagan, R.T., Giannakakis, G., Flytzani-Stephanopoulos, M., and Sykes, E.C.H. (2020). Single-atom alloy catalysis. Chem. Rev. *120*, 12044–12088. https://doi.org/10.1021/acs.chemrev.0c00078.
12. Zaera, F. (2022). Designing sites in heterogeneous catalysis: are we reaching selectivities competitive with those of homogeneous catalysts? Chem. Rev. *122*, 8594–8757. https://doi.org/10.1021/acs.chemrev.1c00905.
13. Wong, A., Liu, Q., Griffin, S., Nicholls, A., and Regalbuto, J.R. (2017). Synthesis of ultrasmall, homogeneously alloyed, bimetallic nanoparticles on silica supports. Science *358*, 1427–1430. https://doi.org/10.1126/science.aao6538.
14. Kaiser, S.K., Chen, Z., Faust Akl, D., Mitchell, S., and Pérez-Ramírez, J. (2020). Single-atom catalysts across the periodic table. Chem. Rev. *120*, 11703–11809. https://doi.org/10.1021/acs.chemrev.0c00576.
15. Wegener, E.C., Bukowski, B.C., Yang, D., Wu, Z., Kropf, A.J., Delgass, W.N., Greeley, J., Zhang, G., and Miller, J.T. (2020). Intermetallic compounds as an alternative to single-atom alloy catalysts: geometric and electronic structures from advanced X-ray spectroscopies and computational studies. ChemCatChem *12*, 1325–1333. https://doi.org/10.1002/cctc.201901869.
16. Zhang, T., Walsh, A.G., Yu, J., and Zhang, P. (2021). Single-atom alloy catalysts: structural analysis, electronic properties and catalytic activities. Chem. Soc. Rev. *50*, 569–588. https://doi.org/10.1039/d0cs00844c.
17. Guo, Y., Wang, M., Zhu, Q., Xiao, D., and Ma, D. (2022). Ensemble effect for single-atom, small cluster and nanoparticle catalysts. Nat. Catal. *5*, 766–776. https://doi.org/10.1038/s41929-022-00839-7.
18. Chen, Y., Lin, J., Pan, Q., Liu, X., Ma, T., and Wang, X. (2023). Inter-metal interaction of dual-atom catalysts in heterogeneous catalysis. Angew. Chem. Int. Ed. *62*, e202306469. https://doi.org/10.1002/anie.202306469.
19. Jin, H., Song, W., and Cao, C. (2023). An overview of metal density effects in single-atom catalysts for thermal catalysis. ACS Catal. *13*, 15126–15142. https://doi.org/10.1021/acscatal.3c03928.
20. Wang, H., Yang, T., Wang, J., Zhou, Z., Pei, Z., and Zhao, S. (2024). Coordination engineering in single-site catalysts: general principles, characterizations, and recent advances. Chem *10*, 48–85. https://doi.org/10.1016/j.chempr.2023.08.014.
21. Benkovic, S.J., and Hammes-Schiffer, S. (2003). A perspective on enzyme catalysis. Science *301*, 1196–1202. https://doi.org/10.1126/science.1085515.
22. Vogt, C., and Weckhuysen, B.M. (2022). The concept of active site in heterogeneous catalysis. Nat. Rev. Chem. *6*, 89–111. https://doi.org/10.1038/s41570-021-00340-y.
23. Wei, H., Liu, X., Wang, A., Zhang, L., Qiao, B., Yang, X., Huang, Y., Miao, S., Liu, J., and Zhang, T. (2014). FeO_x-supported platinum single-atom and pseudo-single-atom catalysts for chemoselective hydrogenation of functionalized nitroarenes. Nat. Commun. *5*, 5634. https://doi.org/10.1038/ncomms6634.
24. Carta, D., Mountjoy, G., Apps, R., and Corrias, A. (2012). Effect of the support on the formation of FeCo alloy nanoparticles in an SBA-16 mesoporous silica matrix: an X-ray absorption spectroscopy study. J. Phys. Chem. C *116*, 12353–12365. https://doi.org/10.1021/jp302927t.
25. Jeong, H., Kwon, O., Kim, B.-S., Bae, J., Shin, S., Kim, H.-E., Kim, J., and Lee, H. (2020). Highly durable metal ensemble catalysts with full dispersion for automotive applications beyond single-atom catalysts. Nat. Catal. *3*, 368–375. https://doi.org/10.1038/s41929-020-0427-z.
26. Li, X., Pereira-Hernández, X.I., Chen, Y., Xu, J., Zhao, J., Pao, C.-W., Fang, C.-Y., Zeng, J., Wang, Y., Gates, B.C., et al. (2022). Functional CeO_x

nanoglues for robust atomically dispersed catalysts. Nature *611*, 284–288. https://doi.org/10.1038/s41586-022-05251-6.

27. Cabot, A., Puntes, V.F., Shevchenko, E., Yin, Y., Balcells, L., Marcus, M.A., Hughes, S.M., and Alivisatos, A.P. (2007). Vacancy coalescence during oxidation of iron nanoparticles. J. Am. Chem. Soc. *129*, 10358–10360. https://doi.org/10.1021/ja072574a.

28. Jiang, M., Liu, W., Yang, X., Jiang, Z., Yao, T., Wei, S., and Peng, X. (2015). Pt/Fe_3O_4 core/shell triangular nanoprisms by heteroepitaxy: facet selectivity at the Pt-Fe_3O_4 interface and the Fe_3O_4 outer surface. ACS Nano *9*, 10950–10960. https://doi.org/10.1021/acsnano.5b04130.

29. Chen, W., Gao, W., Tu, P., Robert, T., Ma, Y., Shan, H., Gu, X., Shang, W., Tao, P., Song, C., et al. (2018). Neighboring Pt atom sites in an ultrathin FePt nanosheet for the efficient and highly CO-tolerant oxygen reduction reaction. Nano Lett. *18*, 5905–5912. https://doi.org/10.1021/acs.nanolett.8b02606.

30. Lan, X., and Wang, T. (2020). Highly selective catalysts for the hydrogenation of unsaturated aldehydes: a review. ACS Catal. *10*, 2764–2790. https://doi.org/10.1021/acscatal.9b04331.

31. Mao, S., Wang, Z., Luo, Q., Lu, B., and Wang, Y. (2023). Geometric and electronic effects in hydrogenation reactions. ACS Catal. *13*, 974–1019. https://doi.org/10.1021/acscatal.2c05141.

32. Aleksandrov, H.A., Neyman, K.M., Hadjiivanov, K.I., and Vayssilov, G.N. (2016). Can the state of platinum species be unambiguously determined by the stretching frequency of an adsorbed CO probe molecule? Phys. Chem. Chem. Phys. *18*, 22108–22121. https://doi.org/10.1039/C6CP03988J.

33. Ding, K., Gulec, A., Johnson, A.M., Schweitzer, N.M., Stucky, G.D., Marks, L.D., and Stair, P.C. (2015). Identification of active sites in CO oxidation and water-gas shift over supported Pt catalysts. Science *350*, 189–192. https://doi.org/10.1126/science.aac6368.

34. Liu, J., Lucci, F.R., Yang, M., Lee, S., Marcinkowski, M.D., Therrien, A.J., Williams, C.T., Sykes, E.C.H., and Flytzani-Stephanopoulos, M. (2016). Tackling CO poisoning with single-atom alloy catalysts. J. Am. Chem. Soc. *138*, 6396–6399. https://doi.org/10.1021/jacs.6b03339.

35. Marcinkowski, M.D., Darby, M.T., Liu, J., Wimble, J.M., Lucci, F.R., Lee, S., Michaelides, A., Flytzani-Stephanopoulos, M., Stamatakis, M., and Sykes, E.C.H. (2018). Pt/Cu single-atom alloys as coke-resistant catalysts for efficient C–H activation. Nat. Chem. *10*, 325–332. https://doi.org/10.1038/nchem.2915.

36. Zhang, X., Cui, G., Feng, H., Chen, L., Wang, H., Wang, B., Zhang, X., Zheng, L., Hong, S., and Wei, M. (2019). Platinum-copper single atom alloy catalysts with high performance towards glycerol hydrogenolysis. Nat. Commun. *10*, 5812. https://doi.org/10.1038/s41467-019-13685-2.

37. Delbecq, F., and Sautet, P. (1996). Electronic and chemical properties of the $Pt_{80}Fe_{20}$(111) alloy surface: a theoretical study of the adsorption of atomic H, CO, and unsaturated molecules. J. Catal. *164*, 152–165. https://doi.org/10.1006/jcat.1996.0371.

38. Nakaya, Y., Hirayama, J., Yamazoe, S., Shimizu, K.-I., and Furukawa, S. (2020). Single-atom Pt in intermetallics as an ultrastable and selective catalyst for propane dehydrogenation. Nat. Commun. *11*, 2838. https://doi.org/10.1038/s41467-020-16693-9.

39. Chen, S., Zhao, Z.-J., Mu, R., Chang, X., Luo, J., Purdy, S.C., Kropf, A.J., Sun, G., Pei, C., Miller, J.T., et al. (2021). Propane dehydrogenation on single-site [$PtZn_4$] intermetallic catalysts. Chem *7*, 387–405. https://doi.org/10.1016/j.chempr.2020.10.008.

40. Siani, A., Alexeev, O.S., Lafaye, G., and Amiridis, M.D. (2009). The effect of Fe on SiO_2-supported Pt catalysts: structure, chemisorptive, and catalytic properties. J. Catal. *266*, 26–38. https://doi.org/10.1016/j.jcat.2009.05.013.

41. Kennedy, G., Baker, L.R., and Somorjai, G.A. (2014). Selective amplification of C=O bond hydrogenation on Pt/TiO_2: catalytic reaction and sum-frequency generation vibrational spectroscopy studies of crotonaldehyde hydrogenation. Angew. Chem. Int. Ed. *53*, 3405–3408. https://doi.org/10.1002/anie.201400081.

42. Neumann, S., Doebler, H.H., Keil, S., Erdt, A.J., Gutsche, C., Borchert, H., Kolny-Olesiak, J., Parisi, J., Bäumer, M., and Kunz, S. (2020). Effects of particle size on strong metal-support interactions using colloidal "surfactant-free" Pt nanoparticles supported on Fe_3O_4. ACS Catal. *10*, 4136–4150. https://doi.org/10.1021/acscatal.9b04367.

43. Karim, W., Spreafico, C., Kleibert, A., Gobrecht, J., VandeVondele, J., Ekinci, Y., and van Bokhoven, J.A. (2017). Catalyst support effects on hydrogen spillover. Nature *541*, 68–71. https://doi.org/10.1038/nature20782.

44. Wei, J., Qin, S.-N., Liu, J.-L., Ruan, X.-Y., Guan, Z., Yan, H., Wei, D.-Y., Zhang, H., Cheng, J., Xu, H., et al. (2020). In situ Raman monitoring and manipulating of interfacial hydrogen spillover by precise fabrication of Au/TiO_2/Pt sandwich structures. Angew. Chem. Int. Ed. *59*, 10343–10347. https://doi.org/10.1002/anie.202000426.

45. Tan, M., Yang, Y., Yang, Y., Chen, J., Zhang, Z., Fu, G., Lin, J., Wan, S., Wang, S., and Wang, Y. (2022). Hydrogen spillover assisted by oxygenate molecules over nonreducible oxides. Nat. Commun. *13*, 1457. https://doi.org/10.1038/s41467-022-29045-6.

46. Katona, G.L., Vladymyrskyi, I.A., Makogon, I.M., Sidorenko, S.I., Kristály, F., Daróczi, L., Csik, A., Liebig, A., Beddies, G., Albrecht, M., et al. (2014). Grain boundary diffusion induced reaction layer formation in Fe/Pt thin films. Appl. Phys. A *115*, 203–211. https://doi.org/10.1007/s00339-013-7949-z.

47. Chittari, B.L., and Kumar, V. (2015). Atomic structure, alloying behavior, and magnetism in small Fe-Pt clusters. Phys. Rev. B *92*, 125442. https://doi.org/10.1103/PhysRevB.92.125442.

48. Chen, M., Kumar, D., Yi, C.-W., and Goodman, D.W. (2005). The promotional effect of gold in catalysis by palladium-gold. Science *310*, 291–293. https://doi.org/10.1126/science.1115800.

49. Ravel, B., and Newville, M. (2005). ATHENA, ARTEMIS, HEPHAESTUS: data analysis for X-ray absorption spectroscopy using IFEFFIT. J. Synchrotron Radiat. *12*, 537–541. https://doi.org/10.1107/S0909049505012719.

50. Wang, Y., and Wöll, C. (2017). IR spectroscopic investigations of chemical and photochemical reactions on metal oxides: bridging the materials gap. Chem. Soc. Rev. *46*, 1875–1932. https://doi.org/10.1039/C6CS00914J.

51. Kresse, G., and Furthmüller, J. (1996). Efficiency of ab-initio total energy calculations for metals and semiconductors using a plane-wave basis set. Comput. Mater. Sci. *6*, 15–50. https://doi.org/10.1016/0927-0256(96)00008-0.

52. Kresse, G., and Furthmüller, J. (1996). Efficient iterative schemes for ab initio total-energy calculations using a plane-wave basis set. Phys. Rev. B Condens. Matter *54*, 11169–11186. https://doi.org/10.1103/physrevb.54.11169.

53. Tkatchenko, A., and Scheffler, M. (2009). Accurate molecular van der Waals interactions from ground-state electron density and free-atom reference data. Phys. Rev. Lett. *102*, 073005. https://doi.org/10.1103/PhysRevLett.102.073005.

54. Kresse, G., and Joubert, D. (1999). From ultrasoft pseudopotentials to the projector augmented-wave method. Phys. Rev. B *59*, 1758–1775. https://doi.org/10.1103/PhysRevB.59.1758.

55. Henkelman, G., and Jónsson, H. (2000). Improved tangent estimate in the nudged elastic band method for finding minimum energy paths and saddle points. J. Chem. Phys. *113*, 9978–9985. https://doi.org/10.1063/1.1323224.

56. Henkelman, G., Uberuaga, B.P., and Jónsson, H. (2000). A climbing image nudged elastic band method for finding saddle points and minimum energy paths. J. Chem. Phys. *113*, 9901–9904. https://doi.org/10.1063/1.1329672.

57. Kästner, J., and Sherwood, P. (2008). Superlinearly converging dimer method for transition state search. J. Chem. Phys. *128*, 014106. https://doi.org/10.1063/1.2815812.

58. Wang, T., Tian, X.-X., Li, Y.-W., Wang, J., Beller, M., and Jiao, H. (2014). Coverage-dependent CO adsorption and dissociation mechanisms on iron surfaces from DFT computations. ACS Catal. *4*, 1991–2005. https://doi.org/10.1021/cs500287r.

59. Haas, P., Tran, F., and Blaha, P. (2009). Calculation of the lattice constant of solids with semilocal functionals. Phys. Rev. B *79*, 085104. https://doi.org/10.1103/PhysRevB.79.085104.

60. Wang, H., Liu, J.-X., Allard, L.F., Lee, S., Liu, J., Li, H., Wang, J., Wang, J., Oh, S.H., Li, W., et al. (2019). Surpassing the single-atom catalytic activity limit through paired Pt-O-Pt ensemble built from isolated Pt_1 atoms. Nat. Commun. *10*, 3808. https://doi.org/10.1038/s41467-019-11856-9.